Chinese Journal of Natural Medicines

Multimethod-guided discovery of novel α-pyrone dimers with cardiomyocyte-protective activity against cold ischemia injury from the coral-derived *Talaromyces* sp. TJ403-AL05

Hanxiao Zeng, Yaxing Wang, Chenmeng Huang, Rui Jiang, Yongfei Zhang, Zixue Chai, Jiangyang Chi, Yonghui Zhang, Zhengxi Hu

Citation: Hanxiao Zeng, Yaxing Wang, Chenmeng Huang, Rui Jiang, Yongfei Zhang, Zixue Chai, Jiangyang Chi, Yonghui Zhang, Zhengxi Hu, Multimethod-guided discovery of novel α-pyrone dimers with cardiomyocyte-protective activity against cold ischemia injury from the coral-derived *Talaromyces* sp. TJ403-AL05, Chinese Journal of Natural Medicines, 2026, 24(9), 1110-1122. doi: 10.1016/S1875-5364(26)61207-1.

View online: https://doi.org/10.1016/S1875-5364(26)61207-1

Related articles that may interest you

Rapid identification of stigmastane-type steroid saponins from *Vernonia amygdalina* leaf based on α-glucosidase inhibiting activity and molecular networking

Chinese Journal of Natural Medicines. 2022, 20(11), 846-853 https://doi.org/10.1016/S1875-5364(22)60235-8

Talaketides AG, linear polyketides with prostate cancer cytotoxic activity from the mangrove sediment-derived fungus *Talaromyces* sp. SCSIO 41027

Chinese Journal of Natural Medicines. 2024, 22(11), 1047-1056 https://doi.org/10.1016/S1875-5364(24)60659-X

Bioassay-guided isolation of α-Glucosidase inhibitory constituents from *Hypericum sampsonii*

Chinese Journal of Natural Medicines. 2023, 21(6), 443-453 https://doi.org/10.1016/S1875-5364(23)60472-8

Stigmasterol protects human brain microvessel endothelial cells against ischemia-reperfusion injury through suppressing EPHA2 phosphorylation

Chinese Journal of Natural Medicines. 2023, 21(2), 127-135 https://doi.org/10.1016/S1875-5364(23)60390-5

Thirteen new peptaibols with antimicrobial activities from *Trichoderma* sp.

Chinese Journal of Natural Medicines. 2023, 21(11), 868-880 https://doi.org/10.1016/S1875-5364(23)60499-6

New pimarane diterpenoids with antibacterial activity from fungus *Arthrinium* sp. ZS03

Chinese Journal of Natural Medicines. 2024, 22(4), 356-364 https://doi.org/10.1016/S1875-5364(24)60629-1

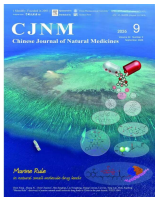
Wechat

Chinese Journal of Natural Medicines 24 (2026) 1110-1122

Contents lists available at ScienceDirect

Chinese Journal of Natural Medicines

journal homepage: www.cjnmcpu.com/



Original article

Multimethod-guided discovery of novel α-pyrone dimers with cardiomyocyte-protective activity against cold ischemia injury from the coral-derived *Talaromyces* sp. TJ403-AL05

Hanxiao Zeng[a,Δ], Yaxing Wang[a,Δ], Chenmeng Huang[e,Δ], Rui Jiang[a], Yongfei Zhang[a], Zixue Chai[a], Jiangyang Chi[b,*], Yonghui Zhang[a,*], Zhengxi Hu[a,c,d,*]

[a] *Hubei Key Laboratory of Natural Medicinal Chemistry and Resource Evaluation, School of Pharmacy, Tongji Medical College, Huazhong University of Science and Technology, Wuhan 430030, China*
[b] *State Key Laboratory of Biocatalysis and Enzyme Engineering, School of Life Sciences, Hubei University, Wuhan 430062, China*
[c] *Hubei Jiangxia Laboratory, Wuhan 430200, China*
[d] *Hubei Shizhen Laboratory, Wuhan 430061, China*
[e] *Department of Oncology, The First Affiliated Hospital of Henan University, Kaifeng 475001, China*

ARTICLE INFO

Article history:
Received 27 October 2025
Revised 14 December 2025
Accepted 16 January 2026
Available online 20 September 2026

Keywords:
Talaromyces sp.
α-Pyrone dimers
GNPS molecular networking
HSQC-based SMART and DeepSAT
Cardioprotective activity

ABSTRACT

Guided by molecular networking, HSQC-based DeepSAT, and SMART analyses, a chemical investigation of the coral-derived fungus *Talaromyces* sp. TJ403-AL05 led to the isolation and identification of taladipyrones A–I (**1**–**9**), a series of new α-pyrone dimers with four distinct skeletons. Among these, compounds **1** and **9** represented two unprecedented classes of rearranged α-pyrone dimers, and compounds **5**–**7** were the first talarolactone-type dimers obtained as racemates. Extensive spectroscopic analysis, quantum chemical calculations, and X-ray diffraction analysis were used to determine their structures, including each enantiomer of racemic compounds **5**–**8** after chiral HPLC resolution. In human cardiomyocytes (AC16), compounds **1**–**6** and **8**–**9** attenuated injury caused by 24 h cold ischemia (CI) at 40 μmol·L^{-1}. Moreover, compound **2** could improve CI-induced disruption of redox homeostasis *via* activation of the PI3K/AKT signaling pathway, representing the first fungal polyketide with such cardioprotective activity.

1. Introduction

The exceptional chemical diversity of natural products underpins their capacity to interact with a wide range of biological targets, making them a crucial source of first-in-class drugs [1]. In this context, microorganisms stand as a premier reservoir for drug discovery, providing structurally complex and synthetically challenging scaffolds [2, 3]. Among filamentous fungi, the genus *Talaromyces*, which was established to accommodate the teleomorphic forms of certain *Penicillium* species [4], is particularly noteworthy. Similar to *Penicillium*, *Talaromyces* possesses abundant biosynthetic gene clusters that produce a remarkable array of secondary metabolites, including alkaloids [5, 6], terpenes [7, 8], and polyketides [9, 10]. Notably, recent studies have increasingly highlighted the ability of *Talaromyces* to yield metabolites with exceptional structural novelty and potent bioactivities, such as hypoglycemic activity [11, 12], anti-inflammatory [13, 14], and anticancer [15-17] activities, thereby establishing its status as a valuable source of lead compounds.

As the important secondary metabolites of *Talaromyces* species, α-pyrone derivatives displayed diverse bioactivities, including immunosuppressive activity, anti-inflammatory activity, and inhibitory activity against xanthine oxidase [18-22]. Motivated by the widespread bioactivities of pyrone derivatives, Global Natural Products Social Molecular Networking (GNPSMN) was applied to rapidly screen a panel of fungal isolates [23], leading to identification of an α-pyrone-producing strain, *Talaromyces* sp. TJ403-AL05. The molecular network of this strain featured a cluster containing one node annotated as a known α-pyrone monomer (annularin A [24]) based on matches in both the GNPS spectral library and our in-house MS/MS library, whereas the remaining nodes in that cluster lacked annotations as shown in Fig. 1A, suggesting previously undescribed pyrone derivatives [25]. Although MN facilitates targeted isolation of novel natural products and enabled rapid dereplication of known ones [26], the approach suffered from inherent limitations. For instance, LC-MS/MS-based networking could generate spurious nodes and edges due to chromatographic coelution, chimeric spectra or background noise [27]. Moreover, even within closely related congeneric series, subtle structural variations such as glycosides and their aglycones would produce significant deviations in clustering and edge connectivity [28]. These effects could be partially mitigated by feature-based molecular networking (FBMN) [27], building block-based molecular networking (BBMN) [29, 30], and simulated MS/MS-guided molecular networking (SMMN) [31], which emphasize MS^1 feature

* Corresponding author.
E-mail addresses: chijiangyang@163.com (J. Chi); zhangyh@mails.tjmu.edu.cn (Y. Zhang); hzx616@126.com (Z. Hu)
Δ These authors contributed equally to this work.

https://doi.org/10.1016/S1875-5364(26)61207-1
Copyright © 2026, China Pharmaceutical University. Published by Elsevier B.V. All rights are reserved.

alignment, building-block diagnostics, or *in silico* predicted spectra, yet precise selection of diagnostic product ions and neutral losses for targeted isolation remains challenging given the diversity and complexity of natural product scaffolds [32].

To overcome these limitations, NMR-based approaches have been increasingly adopted in recent years to provide orthogonal evidence for natural products targeted discovery [33-36]. In this study, pre-fractionated crude extracts were analyzed using HSQC spectroscopy, and the data were interpreted using two HSQC-based annotators: DeepSAT [37] and SMART [38]. Because these tools were trained in different ways for structure prediction, running both was expected to be insightful and to provide complementary results [39]. This integrated approach guided the targeted isolation of a series of *α*-pyrone dimers, designated taladipyrones A–I (**1**–**9**). Among them, compound **1** possessed an unprecedented skeleton featuring a congested 6/6/5/6 ring system, and compound **9** was its biosynthetically related C-8–C-13 cleavage derivative. Herein, the isolation, structural elucidation, and cardioprotective activity against cold ischemia injury of these compounds (Fig. 2) were described.

2. Results and discussion

The required HSQC data were extracted and uploaded into the DeepSAT platform (https://deepsat.ucsd.edu/) and the SMART 2.1 platform (http://smart.ucsd.edu/classic) in the CSV file. The DeepSAT analysis of Fr. E3 (Fig. 1B) yielded only two low-confidence candidates, as expected for novel scaffolds, yet consistently classified the major constituents as cyclic polyketides. Complementarily, the result of SMART analysis (Fig. 1C) proposed structurally diverse candidates, six out of the top eight compounds contained an *α*-pyrone substructure. Similar annotation patterns were also observed in Fr. E4. This convergent evidence supported the presence of cyclic polyketides featuring *α*-pyrone moiety, prompting the prioritization of subfractions E3 and E4 for targeted isolation to obtain novel derivatives.

Compound **1** was isolated as a colorless crystal with a molecular formula of $C_{18}H_{22}O_6$ as inferred from the HR-ESI-MS data, suggesting eight degrees of unsaturation. The ^{1}H NMR data (Table 1) disclosed the characteristic signals attributed to two methyl doublets at δ_H 1.14 (d, J = 6.6 Hz, H_3-12), δ_H 1.34 (d, J = 6.0 Hz, H_3-18); two methyl singlets at δ_H 1.37 (H_3-14) and 3.79 (H_3-20); two oxygenated methines at δ_H 4.92 (dq, J = 9.7, 6.6 Hz, H-11) and 3.79 (m, H-17); and one olefinic proton at δ_H 5.39 (s, H-3). Interpretation of the ^{13}C NMR (Table 1) and HSQC data revealed a total of 18 carbon signals, which were attributable to one ketone carbonyl carbon, one ester carbonyl carbon, four olefinic carbons (including one protonated), two sp^3 non-protonated carbons, three sp^3 methine carbons, three sp^3 methylene carbons and four methyl carbons (including one oxygenated). Combined with the above data analyses, two carbon–carbon double bonds and two carbonyl groups accounted for four of the eight unsaturation units, illustrating the presence of a tetracyclic ring system for **1**.

Detailed dissections of the 1D NMR data and HMBC spectrum (Fig. 3) revealed that **1** possessed one *α*-pyrone moiety (ring A), as evidenced by the diagnostic HMBC correlations from H_3-20 to C-4 and from H-3 to C-2, C-4 and C-5, as well as the typical chemical shift values of C-2 (δ_C 163.9) and C-10 (δ_C 154.3) [40, 41]. Other fragments and their connections were further clarified by the remaining ^{1}H–^{1}H COSY and HMBC correlations (Fig. 3). Analysis of the ^{1}H–^{1}H COSY spectrum revealed three continuous spin-spin coupling systems: H_2-6/H_2-7, H-9/H-11/H_3-12 and H_2-16/H-17/H_3-18. A cyclohexane ring (ring B) connected with ring A through the shared C-5–C-10 bond was inferred by the HMBC correlations from H_2-6 to C-5, C-8 and C-10, from H_2-7 to C-8 and C-9, and from H-9 to C-10. Additionally, in the HMBC spectrum, correlations observed from H_2-16 to C-8 and C-15, from H-17 to C-13 and C-15, and from H_2-7 to C-15 and C-13 established that ring B and a *γ*-pyrone ring (ring C) bearing a methyl linked to C-13 were spiro-fused at C-8. Furthermore, the remaining ring was assigned to be a tetrahydrofuran ring (ring D) fused to rings B and C *via* C-8–C-9 and C-8–C-13, respectively. This assignment was supported by comprehensive analysis of the molecular formula, the key chemical shift value of the quaternary carbon at C-13 (δ_C 111.1), and the HMBC correlations from H-11 to C-8 and C-10. The methyl groups 12-CH_3 and 18-CH_3 were placed at C-11 and C-17, respectively, based on the ^{1}H–^{1}H COSY data described above. Therefore, the planar structure of **1** was defined.

The partial relative configuration of **1** was assigned by analysis of its NOESY data (Fig. 4), of which the correlation between H_3-14 and H_2-7 revealed that C-7–C-8 bond and 14-CH_3 were placed on the same side. However, the unambiguous assignment of the remaining stereocenters by NOESY spectrum alone was challenging due to the presence of the consecutive quaternary

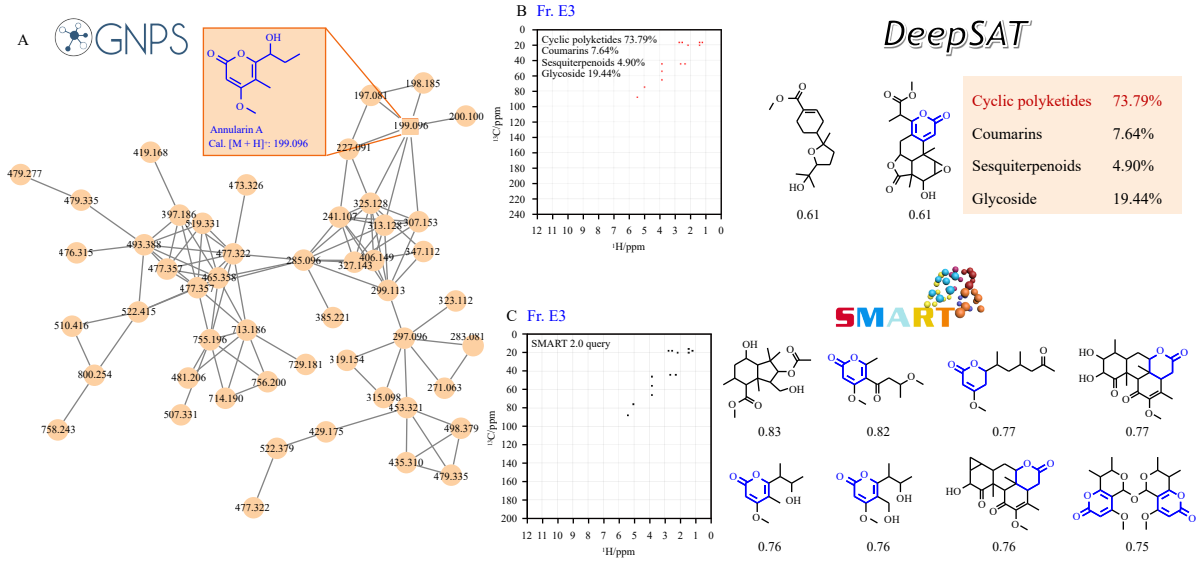


Fig. 1 GNPS molecular networking, DeepSAT and SMART analysis of the rice fermentation products of *Talaromyces* sp. TJ403-AL05. (A) Molecular networking analysis of the ethyl acetate (EtOAc) crude. (B) DeepSAT-based analysis of the HSQC spectrum of Fr. E3 and identification of all cosine-similarity compounds. (C) SMART-based analysis of the HSQC spectrum of Fr. E3 and planar structures of top eight compounds based on the cosine similarity score.

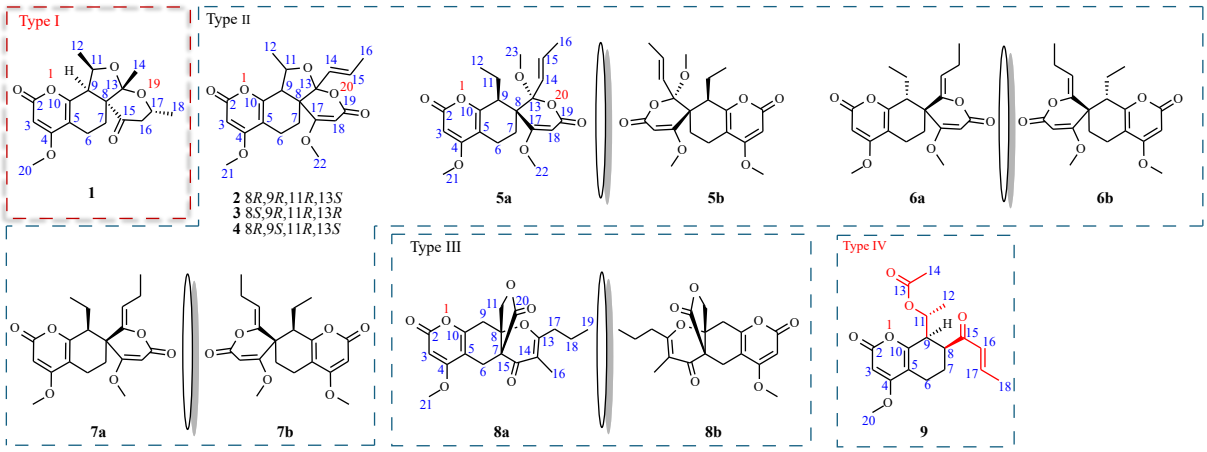


Fig. 2 Chemical structures of taladipyrones A–I (**1**–**9**).

Table 1 ^{1}H NMR and ^{13}C NMR data of compounds **1**–**3** (*J* in Hz).

No.	1		2		3	
	δ_C [a,d]	δ_H [a,c]	δ_C [a,d]	δ_H [a,c]	δ_C [b,d]	δ_H [b,c]
2	163.9 C		164.0 C		166.4 C	
3	88.4 CH	5.39 s	87.3 CH	5.42 s	89.1 CH	5.62 s
4	169.7 C		169.9 C		171.8 C	
5	110.1 C		108.4 C		111.7 C	
6	18.6 CH_2	2.72 dddd (17.5, 11.9, 6.1, 1.6); 2.52 ddd (17.5, 6.1, 1.6)	21.3 CH_2	2.67 m; 2.48 m	20.8 CH_2	2.75 dddd (17.7, 11.3, 6.4, 1.6); 2.65 ddd (17.7, 7.4, 1.6)
7	22.0 CH_2	2.12 ddt (13.5, 6.1, 1.6); 1.41 m	27.8 CH_2	2.05 m; 1.89 ddd (13.5, 11.3, 7.5)	24.8 CH_2	2.00 m; 1.61 ddd (14.5, 11.3, 7.4)
8	61.2 C		47.3 C		51.6 C	
9	46.7 CH	3.79 m	46.0 CH	3.66 br d (7.9)	49.7 CH	3.54 d (10.0)
10	154.3 C		156.3 C		155.6 C	
11	76.5 CH	4.92 dq (9.7, 6.6)	73.3 CH	4.60 m	78.2 CH	4.81 m
12	18.2 CH_3	1.14 d (6.6)	17.8 CH_3	1.24 d (6.6)	18.1 CH_3	1.17 d (6.6)
13	111.1 C		108.5 C		113.9 C	
14	17.5 CH_3	1.37 s	126.3 CH	5.63 dq (15.2, 1.6)	124.3 CH	5.62 dq (15.4, 1.8)
15	208.3 C		132.4 CH	6.10 dq (15.2, 6.6)	133.2 CH	6.08 dq (15.4, 6.6)
16	45.2 CH_2	2.63 dd (14.4, 11.5); 2.26 dd (14.4, 2.7)	17.4 CH_3	1.78 dd (6.6, 1.6)	17.8 CH_3	1.76 dd (6.7, 1.8)
17	67.3 CH	3.79 m	175.1 C		178.8 C	
18	22.2 CH_3	1.34 d (6.0)	91.7 CH	5.28 s	89.5 CH	5.23 s
19			164.0 C		167.2 C	
20	56.2 CH_3	3.79 s				
21			56.2 CH_3	3.81 s	57.3 CH_3	3.91 s
22			56.2 CH_3	3.60 s	57.7 CH_3	3.74 s

[a] In $CDCl_3$; [b] in CD_3OD; [c] recorded at 400 MHz; [d] recorded at 100 MHz; "m" means overlapped or multiplet with other signals.

carbons (like C-8 and C-13) and the oxygen atoms. Finally, a suitable single crystal was obtained and then subjected to single-crystal X-ray diffraction analysis with Cu Kα (Fig. 5), which confirmed the absolute configuration to be 8*S*,9*R*,11*R*,13*S*,17*R*.

Compound **2**, isolated as a colorless crystal, had a molecular formula of $C_{20}H_{22}O_7$ based on its HR-ESI-MS data, requiring ten degrees of unsaturation. Its ^{13}C NMR data (Table 1), combined with HSQC spectrum, exhibited the presence of signals for four olefinic methine protons, two sp^3 methine protons (including one oxygenated), and four methyl (including two oxygenated) protons. In addition, eight non-protonated carbons (six sp^2 carbons and two sp^3 carbons) and two methylene carbons were observed in the ^{13}C NMR spectrum. Comparison of the NMR data of **2** with those of talarolactone A showed high similarity [42], suggesting that they possessed the identical carbocyclic core. The only difference between their planar structures was that the hydroxy group at C-15 in talarolactone A was eliminated to the $\Delta^{14(15)}$ double bond in compound **2**, which could be confirmed by the molecular for-

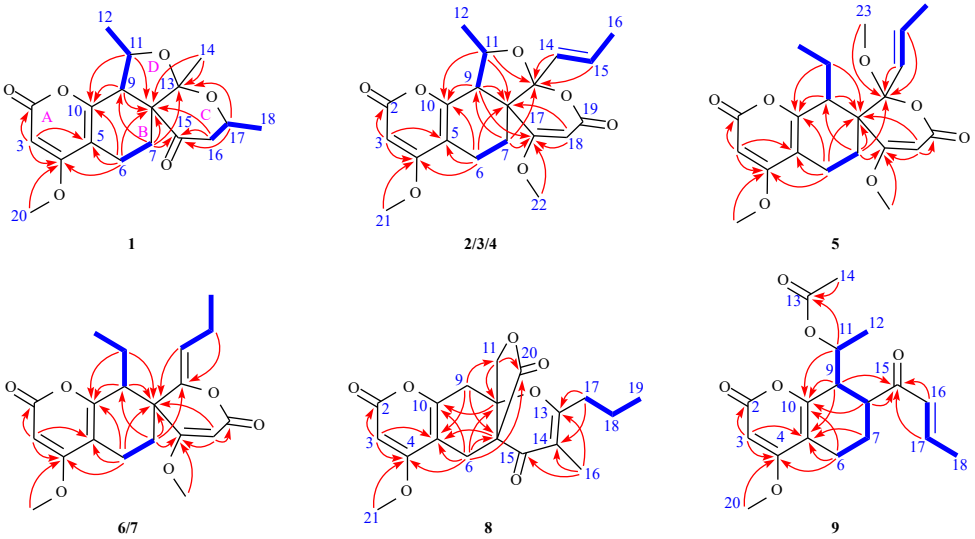


Fig. 3 Key ^{1}H–^{1}H COSY (blue lines) and HMBC (red arrows) correlations of **1**–**9**.

mula and the HMBC correlations (Fig. 3) from H-14 and H-15 to C-13. The *E*-configuration of $\Delta^{14(15)}$ was determined based on the large coupling constant between H-14 and H-15 (^{3}J = 15.1 Hz). The NOESY correlations (Fig. 4) of H-9/H-11, H_2-7/H-14, and H-9/H-7α suggested that H-9, H-11, C-7–C-8 bond and C-13–C-14 bond were established as α-oriented. Furthermore, the assignment of an 8*R*,9*R*,11*R*,13*S* absolute configuration of **2** was corroborated by a single-crystal X-ray diffraction analysis (Fig. 5) with a Flack parameter of 0.00(3).

Compounds **3** and **4** were both purified as white, amorphous powders and shared the same molecular formula, planar structure and *E*-configuration of $\Delta^{14(15)}$ double bond with compound **2** by analysis of the HR-ESI-MS and 1D/2D NMR data. As far as compound **3** was concerned, the coupling constant between H-9 and H-11 in CD_3OD (^{3}J = 10.0 Hz in **3**, and ^{3}J = 9.9 Hz in talarolactone A), the NOESY correlations of H-7β/H_3-12 and H_2-7/H-14, as well as the experimental ECD data were consistent with talarolactone A (Fig. S28) [4], which enabled the assignment of the absolute configuration in **3** to be 8*S*,9*R*,11*R*,13*R*. Likewise, the observed NOESY signals between H_2-7 and H-14, and between H-11 and H-7β in compound **4** indicated the same orientation of H-11, C-7–C-8 bond and C-13–C-14 bond, which enabled to establish the partial configuration as 8S^*,11S^*,13R^*. To further determine the complete relative configuration of **4**, the calculation of NMR data was applied. Consequently, both DP4 + probability analysis and the correlation coefficient (R^2) (Fig. 6A and Table S1) showed that the ^{13}C NMR data of (8S^*,9R^*,11S^*,13R^*)-**4** matched well with the experimental data. Finally, the absolute configuration of **4** was determined as 8*R*,9*S*,11*R*,13*S* by the ECD calculation (Fig. 7).

Compound **5**, obtained as a colorless crystal, possessed the molecular formula $C_{21}H_{26}O_7$ by its HR-ESI-MS data, requiring nine degrees of unsaturation. Detailed analyses of its NMR data (Table 2) suggested that **5** was structurally similar to **2**, except for the absence of the furan ring and the presence of an additional methoxy group attached to C-13. The inference was verified by the HMBC correlations from H_3-23 to C-13, the chemical shifts of C-11 (δ_C 24.6), together with one less degree of unsaturation compared to **2**. The coupling constant between H-14 and H-15 (^{3}J = 15.4 Hz) supported the *E*-configuration of the $\Delta^{14(15)}$ double bond. Further relative configuration was identified as 8R^*,9S^*,13R^* according to the ROESY correlations of H_2-7/H-14, H-9/H-14 (H-15, H_3-16). This conclusion was validated by the single-crystal X-ray diffraction analysis (Fig. 5), which also revealed that **5** was a racemic mixture, with its crystal structure possessing the

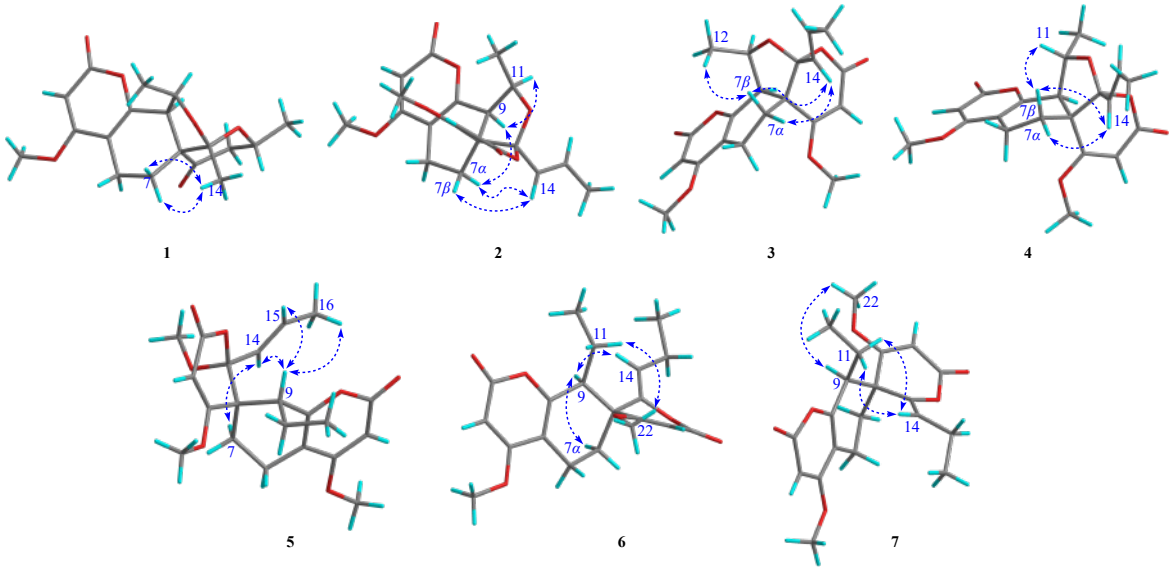


Fig. 4 Key ROESY/NOESY (blue arrows) correlations of **1**–**7**.

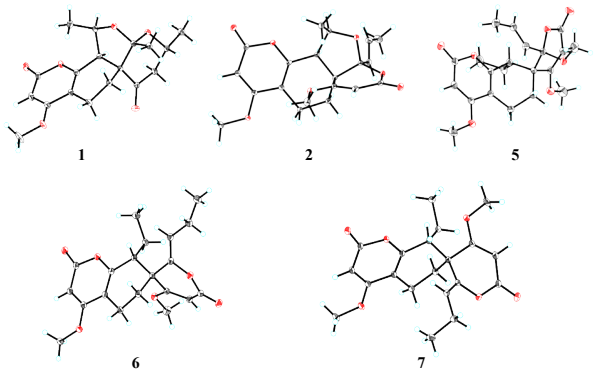


Fig. 5 X-Ray ORTEP drawings of compounds **1**, **2**, and **5**–**7** (displacement ellipsoids were drawn at the 30% probability level).

centrosymmetric space group *P*-1. Thereafter, **5** was separated into two optically pure enantiomers, **5a** and **5b**, on a Chiralpack IG column (Fig. S1). The absolute configurations of **5a** and **5b** were defined to be 8*R*,9*S*,13*R* and 8*S*,9*R*,13*S*, respectively, through comparison of their experimental ECD curves with the calculated curves (Fig. 7).

Compounds **6** and **7** were both obtained as colorless crystals with the identical molecular formula $C_{20}H_{24}O_6$ on the basis of its HR-ESI-MS data. The NMR data (Tables 2 and 3) of both **6** and **7** resembled those of talarolactone C [42], suggesting that they possessed the same carbon framework. The only difference was the disappearance of hydroxy group at C-15 in **6** and **7**, as verified by the ^{1}H–^{1}H COSY correlation between H_2-15 and H_3-16. Therefore, the planar structures of compounds **6** and **7** were identified as the 15-dehydroxy analogues of talarolactone C. Their geometries of the $\Delta^{13(14)}$ double bond were both concluded to be *E* based on the ROESY correlation between H-9 and H-14 in **6**, and between H_2-11 and H-14 in **7**, respectively. Regarding the relative configuration between the chiral carbons, an 8*R**,9*S** configuration in **6** was assigned due to the ROESY correlations of H-9/H-7*α*, H-11/H_3-22 and H-14/H-7*α*, while an 8*S**,9*S** configuration in **7** was established, as evidenced by the ROESY correlation between H-9 and H_3-22. Subsequently, single crystals of compounds **6** and **7** were also successfully obtained, and single-crystal X-ray crystallographic analysis (Fig. 5) revealed that both compounds were racemic mixtures, with crystal structures belonging to the centrosymmetric space groups $P2_1/n$ and *P*-1, respectively. Then, chiral HPLC resolved racemates (±)-**6** and (±)-**7** into optically pure enantiomers **6a**/**6b** and **7a**/**7b** (Fig. S1). Finally, their absolute configurations were established by comparison of the experimental and calculated ECD spectra (Fig. 7): **6a** (8*S*,9*R*), **6b** (8*R*,9*S*), **7a** (8*S*,9*S*), and **7b** (8*R*,9*R*).

Compound **8** was afforded as a colorless oil with the molecular formula $C_{19}H_{20}O_7$ based on its HR-ESI-MS data, indicating ten degrees of unsaturation. The ^{13}C NMR data (Table 3) and HSQC spectrum displayed 19 carbon signals, consisting of three methyls (including one oxygenated), five methylenes (including one oxygenated), one olefinic methines, and ten non-protonated carbons (including one oxygenated, five olefinic, two ester carbonyl groups, and one ketone carbonyl group). The above signals suggested that **8** was an *α*-pyrone derivative [40, 41]. Its 1D NMR data were closely related to those of talapyrone D [43], except for the absence of hydroxy group at C-18, as confirmed by the ^{1}H–^{1}H COSY correlations (Fig. 3) of H_2-17/H_2-18/H_3-19 and the methylene carbon signal of C-18 (δ_C 20.8). Thus, the planar structure of **8** was constructed. The presence of butyrolactone moiety resulted in the caged structure of **8**, which locked the C-8–C-11 and C-7–C-20 bonds in the same orientation [43]. Subsequently, **8** was subjected to chiral separation due to the undetectable Cotton effects in its ECD spectrum. Finally, the racemic mixtures of **8** were successfully separated into **8a** and **8b** on a Chiralpak IG column (Fig. S1). The absolute configurations were assigned as 7*S*,8*S* for **8a** and 7*R*,8*R* for **8b**, based on the agreement between the experimental and calculated ECD curves (Fig. 7).

Compound **9** was purified as a white amorphous powder. Its molecular formula was determined to be $C_{18}H_{22}O_6$ according to its HR-ESI-MS data, requiring eight degrees of unsaturation. The ^{1}H NMR spectrum of **9** presented the diagnostic signals of three olefinic hydrogens, one methoxy group and three methyl groups as showed in Table 3. The ^{13}C NMR and DEPT spectroscopic data (provided in Table 3) displayed 18 carbon signals, which were assignable to four methyls (one methoxy), two methylenes, six methines (one oxygenated and three olefinic), and six non-protonated carbons (two olefinic, one ketone carbonyls, two ester, and one oxygenated). The characteristic chemical shift values of the *α*-pyrone moiety (C-2, δ_C 166.7; C-3, δ_C 88.7; C-4, δ_C 172.5; C-5, δ_C 111.8; C-10, δ_C 158.9), similar to those in compounds **1**–**8**, confirmed its presence in **9** as well. Taken together, the aforementioned moieties, comprising one *α*-pyrone, one ketone carbonyl, one additional double bond, and one extra ester group, accounted for seven of the eight degrees of unsaturation, which demonstrated **9** to be a bicyclic *α*-pyrone derivative.

Detailed analysis of the ^{1}H–^{1}H COSY spectrum revealed two spin coupling systems as shown in Fig. 3. Based on the H_2-6/H_2-7/H-8/H-9/H-11/H_3-12 spin system, the remaining ring in the bicyclic system of **9** was constructed as a cyclohexane ring fused with the pyrone ring *via* the C-5–C-10 bond, supported by the HMBC correlations (Fig. 3) from H_2-6, H_2-7 and H-9 to C-5, and from H_2-6, H-8, and H-9 to C-10. Additionally, the HMBC correlations from H-11 and H_3-14 to C-13 confirmed the presence of an acetyl group located at C-11. Meanwhile, the spin coupling system of H-16/H-17/H_3-18 together with the HMBC correlations from H-8, H-9, H-16 and H-17 to C-15 indicated that an *α*,*β*-unsaturated ketone moiety was connected to C-8. Thus, the planar structure of **9** was constructed.

Comprehensive analysis of the coupling constant and NOESY spectrum allowed to assign the relative configuration of compound **9**. A large coupling constant (*J* = 15.6 Hz) between H-16 and H-17 suggested the $\Delta^{16(17)}$ double bond to be *E*-geometry. Additionally, the Newman projection along the C-9–C-11 bond (Fig. 6C) supported the 9*R**,11*R**-configuration, as supported by the observed ROESY correlations of H_2-7/H-11 and H-8/H_3-12/H-9. Subsequent NMR chemical shift calculations of (8*S**,9*R**,11*R**)-**9** and (8*R**,9*R**,11*R**)-**9** were applied to assign the configuration of C-8. Both DP4 + probability analysis and the correlation coefficient (R^2) (Fig. 6B and Table S2) showed that the NMR data of (8*S**,9*R**,11*R**)-**9** match well with the experimental data. Finally, the absolute configuration of **9** was determined to be 8*S*,9*R*,11*R* by comparing its experimental ECD spectrum with the computational ECD curves (Fig. 7).

Compounds **1** and **9** were two novel *α*-pyrone dimers characterized by different reconstructions of the C/D-ring system. Although their frameworks differed from those of the co-isolated compounds **2**–**8**, they hypothetically originated from the similar pyrone monomers (Scheme 1). Based on the previously proposed biosynthetic pathway [42, 43], the monomers dimerized either through a [4 + 2] Diels–Alder (DA) cycloaddition to furnish type II dimers (**2**–**7**) or *via* a Michael addition to give the type III dimer (**8**). Notably, some of the type II dimers (**5**–**7**) were obtained as racemic mixtures for the first time, which could be attributed to the non-stereoselective DA reaction. The type II skeleton was considered to be the biosynthetic precursor of **1** and **9** because of their shared structural moieties. Initially, hydrolytic opening of one *α*-pyrone ring in the tricyclic type II dimer, followed by keto–enol tautomerization and oxidation reactions, gave intermediate **i**. Subsequently, the intermediate **i**, with a typical *β*-keto-

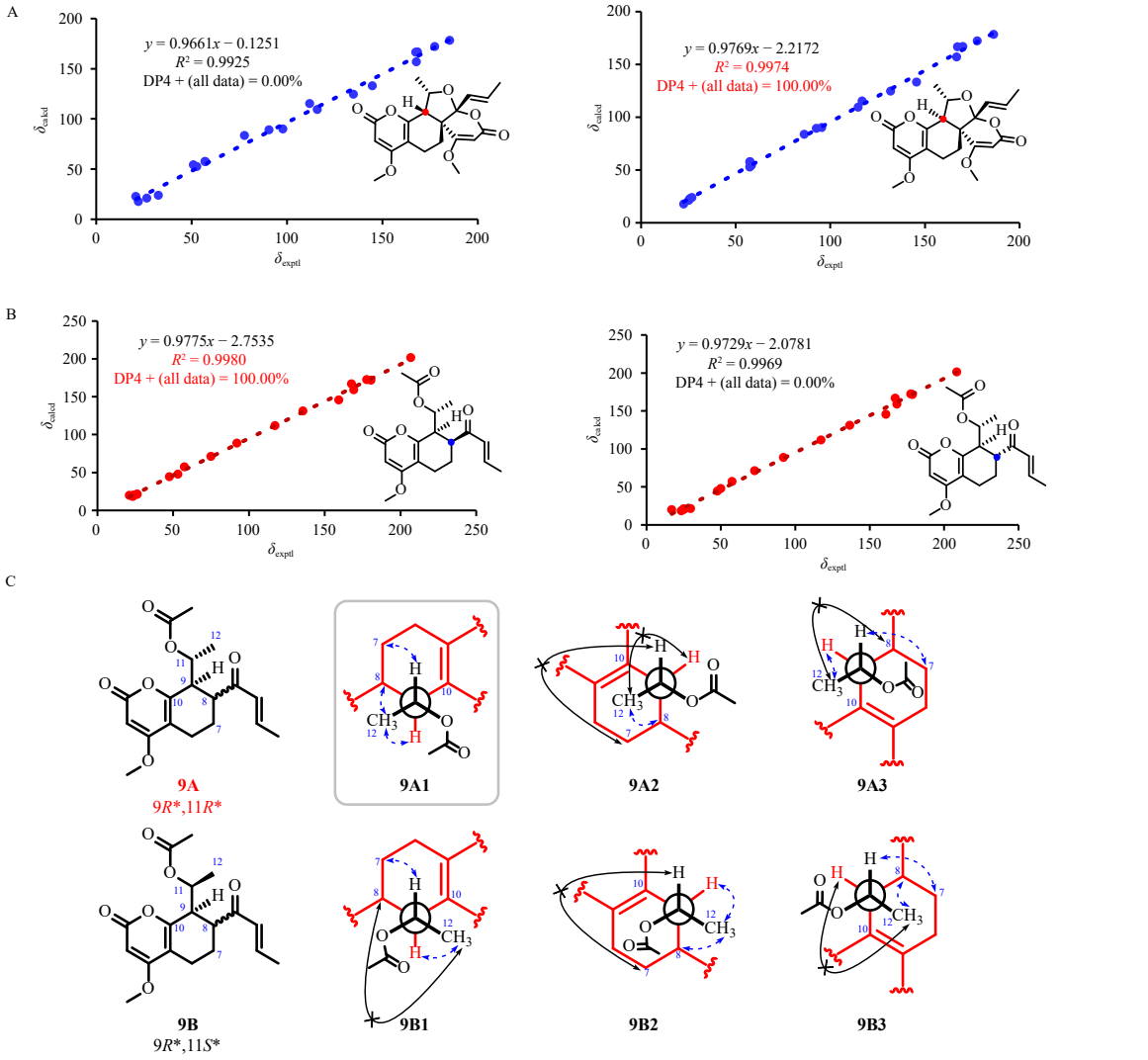


Fig. 6 (A) Theoretical calculations and DP4 + probability analyses of two candidate structures of **4** (the graphs present the linear correlation between the experimental and calculated ^{13}C NMR chemical shifts). (B) Theoretical calculations and DP4 + probability analyses of two candidate structures of **9** (the graphs present the linear correlation between the experimental and calculated ^{13}C NMR chemical shifts). (C) Newman projection analyses of all staggered rotamers viewed along the C-9–C-11 bond for compound **9** and selected ROESY correlations (double blue arrows).

acid moiety, readily underwent decarboxylation to afford intermediate **ii**. Finally, the 5/6 fused ring system in compound **1** was constructed by further intramolecular acetalization and cyclization of intermediate **ii**. Subsequent hydrolysis of the *γ*-pyrone ring and retro-aldol cleavage of the C-8–C-13 bond in compound **1** provided intermediate **iii**, and dehydration then afforded **9**. In summary, compounds **1** and **9** represented the first *α*-pyrone dimers with remodeled C/D rings, plausibly originating from rearrangement of a decarboxylation intermediate derived from the tricyclic type II dimer.

To date, only our research group has reported on natural products isolated from microbiology with protective activity against cold ischemic (CI) injury of the heart, with the previously identified active compounds being exclusively terpenoids and alkaloids [44-47], none of which belonged to the polyketide class. Based on a refined version of previously established method (Fig. 8A) [44], compounds **1**–**9** were evaluated for the cardiomyocyte protective activity against CI to explore more natural cardioprotectants. As a result, compounds **1**–**6** and **8**–**9** demonstrated the ability to attenuate CI-induced damage in AC16 cardiomyocytes at a concentration of 40 μmol·L^{-1} after 24 h (Fig. 8B). Compound **2**, selected for further pharmacological investigation due to its yield and potency, exerted dose-dependent protective effects at both 24 and 48 h post CI (Figs. 8C and 8D). Apoptosis analysis *via* Annexin V/PI staining demonstrated that compound **2** dose-dependently prevented CI-induced apoptosis in AC16 cells (Fig. 8E). Moreover, compound **2** also increased the cell viability after CI following reperfusion (Fig. 8F), further confirmed the protective effect of compound **2** on CI. It has been established that CI upset the balance of redox systems, disturbing mitochondrial function and causing damage to lipids [48-50]. In this study, pretreatment with compound **2** resulted in a marked increase in ATP levels (Fig. 8G) and significantly reduced the release of LDH (Fig. 8H), the level of MDA (Fig. 8I), and ROS generation in a concentration-dependent manner compared to the CI + Vehicle group (Fig. 8J), demonstrating that compound **2** pretreatment alleviated oxidative stress and mitochondrial damage induced by CI. The PI3K/AKT signaling pathway has been proved to play a protective role in ischemia reperfusion injury (IRI) across the heart, brain, lungs, liver, and kidneys, and impart the cardioprotective effects of many drugs in IRI [51-55]. Here, compound **2** increased phosphorylation of PI3K and AKT at 3, 6, and 12 h post CI (Fig. 8K). Consistent with these findings, recent studies have highlighted the broad potential of natural products in treating inflammatory and degenerative diseases by targeting key signaling pathways [56-59]. In conclusion, compound **2** might improve the CI-induced disruption of redox homeostasis by activating PI3K/AKT signal pathway.

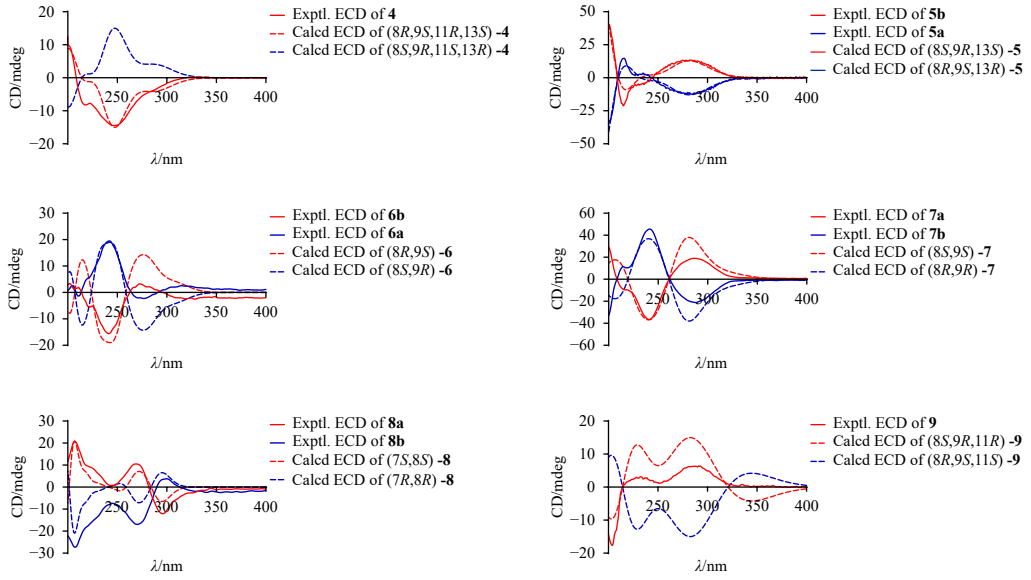


Fig. 7 Experimental and calculated ECD curves of compounds **4**–**9**.

3. Conclusion

In summary, a multimethod workflow integrating GNPS molecular networking with HSQC-based DeepSAT and SMART enabled the targeted discovery of a series of new *α*-pyrone dimers from the coral-derived *Talaromyces* sp. TJ403-AL05. Among them, compounds **1** and **9** represented unprecedented structural classes derived from biosynthetic rearrangement, while com-

Table 2 ^{1}H NMR and ^{13}C NMR data of compounds **4**–**6** (*J* in Hz).

No.	4		5		6	
	δ_C [b,e]	δ_H [b,c]	δ_C [a,f]	δ_H [a,d]	δ_C [a,f]	δ_H [a,d]
2	166.4 C		164.3 C		164.4 C	
3	89.2 CH	5.62 s	87.6 CH	5.38 s	87.9 CH	5.45 s
4	172.2 C		169.7 C		169.8 C	
5	109.3 C		108.3 C		106.7 C	
6	21.1 CH_2	2.79 dddd (17.6, 11.4, 6.7, 1.4); 2.65 ddd (17.6, 7.5, 1.4)	18.3 CH_2	2.48 ddd (14.7, 10.5, 7.5); 2.35 m	18.0 CH_2	2.55 dt (17.4, 7.2); 2.29 dtd (17.4, 7.2, 2.0)
7	23.8 CH_2	1.96 ddt (14.5, 6.7, 1.4); 1.69 m	20.9 CH2	2.35 m; 1.94 m	27.8 CH_2	2.44 ddd (14.4, 7.2, 5.5); 1.78 dt (14.4, 7.2)
8	52.6 C		50.9 C		47.3 C	
9	54.1 CH	3.05 d (7.9)	42.8 CH	2.62 dd (7.4, 5.3)	44.2 CH	2.83 m
10	156.9 C		161.5 C		160.6 C	
11	83.5 CH	4.35 dq (8.0, 6.2)	24.6 CH_2	1.57 m; 1.47 dt (14.4, 7.4)	23.5 CH_2	1.69 m; 1.54 dqd (14.9, 7.5, 3.1)
12	22.7 CH_3	1.57 d (6.2)	12.6 CH_3	0.88 t (7.4)	14.6 CH_3	1.13 t (7.5)
13	115.2 C		107.0 C		148.4 C	
14	124.6 CH	5.57 dq (15.3, 1.6)	125.3 CH	5.03 dq (15.4, 1.8)	113.7 CH	4.91 t (7.5)
15	133.1 CH	6.07 dq (15.3, 6.7)	134.1 CH	6.19 dq (15.4, 6.6)	18.2 CH_2	2.21 p (7.5)
16	17.7 CH_3	1.76 dd (6.7, 1.6)	17.7 CH_3	1.57 dd (6.6, 1.8)	14.0 CH_3	0.94 t (7.5)
17	178.2 C		175.6 C		176.0 C	
18	90.0 CH	5.25 s	90.2 CH	5.22 s	90.1 CH	5.16 s
19	166.8 C		164.6 C		163.3 C	
20						
21	57.3 CH_3	3.90 s	56.2 CH_3	3.82 s	56.2 CH_3	3.82 s
22	57.7 CH_3	3.74 s	56.3 CH	3.75 s	56.6 CH_3	3.69 s
23			51.3 CH_3	3.22 s		

[a] In $CDCl_3$; [b] in CD_3OD; [c] recorded at 400 MHz; [d] recorded at 600 MHz; [e] recorded at 100 MHz; [f] recorded at 150 MHz; "m" means overlapped or multiplet with other signals.

Table 3 ^{1}H NMR and ^{13}C NMR data of compounds **7**–**9** (*J* in Hz).

No.	7		8		9	
	δ_C [a, d]	δ_H [a, b]	δ_C [a, e]	δ_H [a, c]	δ_C [a, e]	δ_H [a, c]
2	164.4 C		165.9 C		166.7 C	
3	87.8 CH	5.45 s	89.0 CH	5.60 s	88.7 CH	5.61 s
4	169.8 C		171.2 C		172.5 C	
5	107.1 C		106.8 C		111.8 C	
6	18.5 CH_2	2.57 dddd (17.2, 5.5, 3.8, 1.4); 2.35 m	23.7 CH_2	3.73 dt (17.5, 1.9); 2.57 dt (17.5, 2.6)	20.2 CH_2	2.46 dddd (17.4, 6.7, 4.1, 1.2); 2.36 dddd (17.4, 8.5, 6.7, 1.5)
7	29.3 CH_2	2.02 m; 1.90 m	53.4 C		21.3 CH_2	2.03 m; 1.92 m
8	47.7 C		86.0 C		47.8 CH	3.29 m
9	43.4 CH	3.22 m	30.8 CH_2	3.15 dd (19.0, 1.9); 3.04 dd (19.0, 2.6)	44.4 CH	3.25 t (4.4)
10	159.8 C		155.2 C		158.9 C	
11	23.2 CH_2	1.86 m; 1.48 dqd (14.8, 7.5, 3.2)	74.6 CH_2	4.63 d (10.4); 4.50 d (10.4)	71.2 CH	5.13 qd (6.6, 4.4)
12	15.0 CH_3	1.10 t (7.5)			19.8 CH_3	1.26 d (6.6)
13	144.0 C		172.1 C		171.7 C	
14	116.3 CH	4.70 t (7.5)	110.2 C		21.2 CH_3	1.95 s
15	18.2 CH_2	2.20 m	184.5 C		201.5 C	
16	14.0 CH_3	0.91 t (7.5)	9.7 CH_3	1.76 s	131.1 CH	6.37 dq (15.6, 1.7)
17	177.0 C		35.3 CH_2	2.41 m	145.7 CH	7.04 dq (15.6, 6.9)
18	89.8 CH	5.17 s	20.8 CH_2	1.64 m	18.4 CH_3	1.94 dd (6.9, 1.6)
19	163.3 C		14.0 CH_3	0.98 t (7.5)		
20			173.5 C		57.2 CH_3	3.89 s
21	56.2 CH_3	3.81 s	57.5 CH_3	3.92 s		
22	56.8 CH_3	3.75 s				

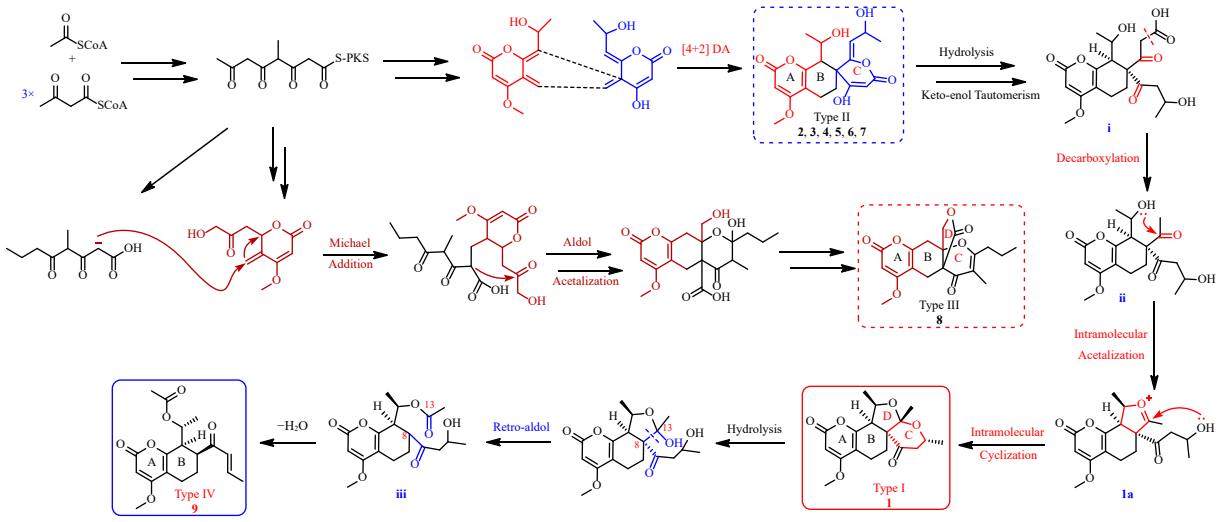
[a] In $CDCl_3$; [b] recorded at 400 MHz; [c] recorded at 600 MHz; [d] recorded at 100 MHz; [e] recorded at 150 MHz; "m" means overlapped or multiplet with other signals.

pounds **5**–**7** were the first report of racemic talarolactone-type dimers. Biological assay revealed that most of these compounds exhibited protective effects against cold ischemia injury in human cardiomyocytes at 40 μmol·L^{-1}, with compound **2** notably ameliorating oxidative stress and mitochondrial dysfunction, possibly through the PI3K/AKT signaling pathway. This work not only enriches the structural diversity of fungal *α*-pyrone dimers but also reports the first polyketide-type fungal natural product with cardioprotective potential against cold ischemia injury, underscoring the potential of fungal secondary metabolites as promising lead compounds for cardioprotection.

4. Experimental

4.1. General experimental procedures

Optical rotations, UV spectra, and ECD data were recorded in MeOH using a PerkinElmer 341 spectropolarimeter (Waltham, MA, USA), a Lambda 35 instrument (PerkinElmer, Waltham, MA,



Scheme 1 Plausible biosynthetic pathway of compounds **1**–**9**.

USA), and a JASCO J-1700 spectrometer (Tokyo, Japan), respectively. HR-ESI-MS data were collected in the positive-ion mode on a MicrOTOF II spectrometer (Bruker Daltonik, Bremen, Germany). The NMR spectroscopy were tested on the AM-400 or AM-600 spectrometer (Bruker Biospin, Fällanden, Switzerland). UHPLC MS/MS analysis was performed using an Agilent 1290 Infinity II coupled with a 6545 Q-TOF mass spectrometer (Wilmington, DE, USA). The chemical shifts (δ) were expressed with reference to the solvent signals for CD_3OD (δ_H 3.31 and δ_C 49.0) and $CDCl_3$ (δ_H 7.26 and δ_C 77.2). Column chromatography (CC) was carried out on silica gel (200–300, 100–200, and 80–120 meshes; Qingdao Marine Chemical Inc., Qingdao, China), ODS (50 μm), and Sephadex LH-20 (40–70 μm, Amersham Pharmacia Biotech AB, Uppsala, Sweden). Fractions were monitored by TLC and spots were visualized by heating silica gel plates sprayed with 10% H_2SO_4 in EtOH. Preparative HPLC was conducted on Sanotac instrument China with a UV detector (Shanghai, China) and a YMC C_{18} column (250 mm × 20 mm). Semipreparative HPLC was performed on an Hitachi HPLC system with a UV detector and a reversed-phase (RP) C_{18} column (10 mm × 250 mm).

4.2. Fungal material

The fungus *Talaromyces* sp. TJ403-AL05 was isolated from an inner part of the coral *Acanthastrea lordhowensis*, which was collected from Xisha Island, China. This strain was authenticated based on the morphology and sequence analysis of the ITS region of rDNA (GenBank Accession No. MK450741.1) and is currently preserved in the culture collection of the College of Pharmacy, Tongji Medical College, Huazhong University of Science and Technology.

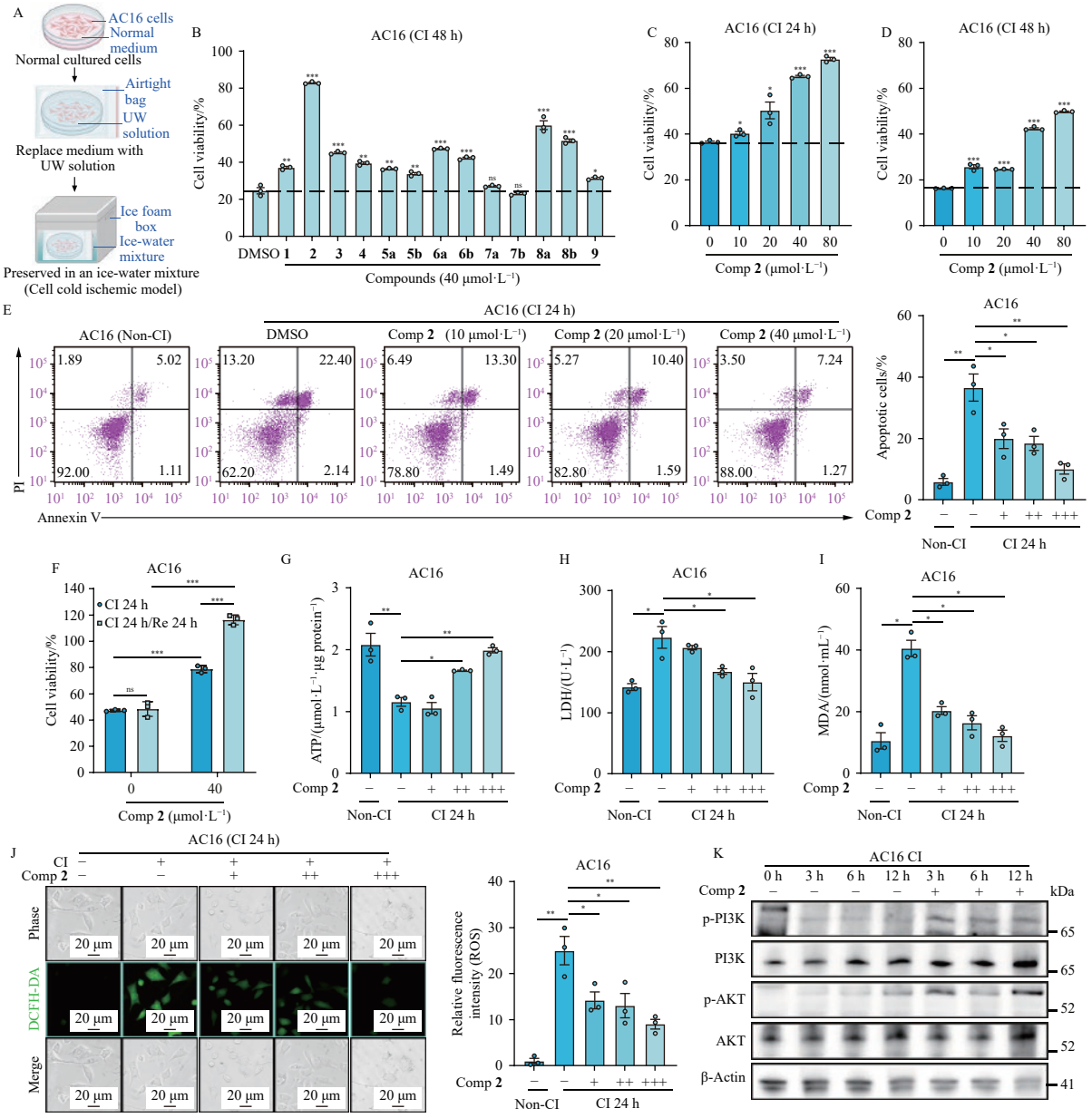


Fig. 8 Compounds protected cold ischemic injury of cardiomyocytes. (A) Schematic diagram of cell cold ischemic (CI) model. (B) Cell counting kit-8 (CCK-8) assay of AC16 cells stored in 0 °C UW solution with or without compounds **1**–**9** was performed at 24 h post cold ischemia. (C and D) Compound **2** acted in a concentration-dependent manner at 24 (C) and 48 (D) h post CI. (E) Annexin V/PI staining kit followed by flow cytometer. (F) CCK-8 assay of AC16 cells stored in 0 °C UW solution with or without compound **2** was performed at 24 h post CI followed by 24 h reperfusion. (G–J) Concentration-dependent effects of compound **2** on oxidative stress and energy metabolism in AC16 cells under CI conditions. The contents of ATP (G), LDH (H), MDA (I) and ROS (J) in AC16 cells. (K) Western blotting analysis of PI3K/AKT signaling pathway expression in AC16 cells stored under CI conditions with or without compound **2** at 3, 6, and 12 h. The results were presented as mean ± SD (n = 3). $^*P < 0.05$, $^{**}P < 0.01$, $^{***}P < 0.001$ *vs* the model group. CI, cold ischemic; Re, reperfusion; Non-CI, non-cold ischemic; SD, standard deviation.

4.3. Molecular networking-based analysis

The LC-MS/MS analysis of crude extract was conducted on an Agilent 1290 Infinity II coupled with a 6545 Q-TOF mass spectrometer (Agilent, USA). The mobile phase was composed of 0.01% TFA in water (*V/V*) and acetonitrile using a gradient elution of 5% acetonitrile at 0 min and then linearly increased to 100% at 17 min, and the flow rate was set as 0.4 mL·min^{-1}. Chromatographic separation was performed on an ZARBOX SB-C_{18} column (4.6 mm × 250 mm, 5-Micron Agilent). The electrospray ionization (ESI) source and positive ion mode were employed. The parameters were as follows: spray voltage, 3000 V; sheath gas pressure, 35 arbitrary units; aux gas pressure, 15 arbitrary units; heater temperature, 300 °C; capillary temperature, 350 °C; S-lens, 60 eV; scan mode, full MS (resolution 70 000) and MS/MS (resolution 17 500); scan range: *m/z* 100–800.

The obtained LC-MS/MS data of the crude extract were converted to mzML format by the ProteoWizard software. The mzML files were then uploaded to the GNPS (https://gnps.ucsd.edu) for classical molecular networking. The product ion and fragment ion mass tolerances were set to 2 Da. After filtering edges to have a cosine score above 0.7 and more than six matched peaks, a network was created. The visualization of the network was achieved using Cytoscape 3.10.3.

4.4. Fermentation, extraction and isolation

Talaromyces sp. TJ403-AL05 was cultured on potato dextrose agar (PDA) at 28 °C for 6 days to prepare the seed cultures. Agar plugs were cut into small pieces and inoculated into 100 Erlenmeyer flasks (1 L), each containing 250 g of rice, 7.5 g sea salt and 250 mL of distilled water, which had been sterilized by autoclave beforehand. After incubating at room temperature for 40 d, fungal growth was stopped by adding 95% EtOH to each flask, and the rice culture was homogenized. The resulting suspension was extracted five times with 95% aqueous EtOH. Afterwards, the solvent was removed under reduced pressure to give an extract, which was suspended in H_2O and repeatedly partitioned with EtOAc. The total extract (520 g) was subjected to silica gel column chromatography (CC) and eluted with a stepwise gradient of petroleum ether (PE)–EtOAc (10∶1, 5∶1, 3∶1, 1∶1, and 0∶1, *V/V*) to yield five main fractions (A–E). Fraction E (38 g) was chromatographed on an ODS column with a MeOH–H_2O gradient (20∶80–80∶20, *V/V*), yielding six subfractions (E1–E6). Subfraction E3 was further separated by silica gel CC (PE–EtOAc, 5∶1–1∶1) to afford five fractions (E3.1–E3.5). Purification of fraction E3.3 by semipreparative HPLC (MeCN–H_2O, 55∶45, *V/V*; 2.0 mL·min^{-1}) directly afforded compound **1** (30.5 mg, t_R 18 min). Fraction E4 was fractionated by silica gel CC (PE–EtOAc, 5∶1–1∶1) to give six subfractions (E4.1–E4.6). Fraction E4.3 was applied to Sephadex LH-20 CC (CH_2Cl_2–MeOH, 1∶1), yielding four fractions (E4.3.1–E4.3.4). Further separation of fraction E4.3.1 on an ODS column with a MeOH–H_2O gradient (40∶60–70∶30) afforded four subfractions (E4.3.1.1–E4.3.1.4). Purification of fraction E4.3.1.1 by semipreparative HPLC (MeCN–H_2O, 49∶51; 2.0 mL·min^{-1}) yielded compounds **9** (1.9 mg, t_R 31 min) and (±)-**8** (2.2 mg, t_R 53 min). Fraction E4.3.1.3 was purified by preparative HPLC (MeCN–H_2O, 60∶40; 8.0 mL·min^{-1}) to yield compounds (±)-**5** (4.6 mg, t_R 27 min), (±)-**6** (4.0 mg, t_R 30 min), and (±)-**7** (4.8 mg, t_R 32 min). Fraction E4.4 was chromatographed on Sephadex LH-20 (CH_2Cl_2–MeOH, 1∶1) to yield three fractions (E4.4.1–E4.4.3). Fraction E4.4.1 was further fractionated on an ODS column with a MeOH–H_2O gradient (20∶80–80∶20) to give five subfractions (E4.4.1.1–E4.4.1.5). Purification of fraction E4.4.1.1 by semipreparative HPLC (MeCN–H_2O, 45∶55; 2.0 mL·min^{-1}) yielded compound **2** (11.8 mg, t_R 38 min). Final purification of fraction E4.4.1.2 by semipreparative HPLC (MeCN–H_2O, 49∶51; 2.0 mL·min^{-1}) afforded compounds **3** (18.2 mg, t_R 34 min) and **4** (14.8 mg, t_R 31 min).

Subsequently, the obtained racemates were subjected to chiral separation. (±)-**5** was separated on a Chiralpak IG column (isocratic MeCN–H_2O, 69∶31; 2.0 mL·min^{-1}) to afford **5a** (2.0 mg, t_R 22 min) and **5b** (1.6 mg, t_R 43 min). (±)-**6** was separated on a Chiralpak IA column (MeCN–H_2O, 60∶40; 0.5 mL·min^{-1}) to yield **6a** (1.2 mg, t_R 20 min) and **6b** (1.1 mg, t_R 29 min). (±)-**7** was separated on a Chiralpak IG column (MeCN–H_2O, 71∶29; 2.0 mL·min^{-1}) to give **7a** (1.7 mg, t_R 19.5 min) and **7b** (1.8 mg, t_R 24 min). (±)-**8** was separated on a Chiralpak IG column (isocratic MeCN–H_2O, 64∶36; 2.0 mL·min^{-1}) to afford **8a** (0.7 mg, t_R 16.5 min) and **8b** (0.8 mg, t_R 20 min).

Taladipyrone A (**1**): colorless prismatic crystals; $[\alpha]_D^{25}$: +93 (*c* 0.10, MeOH); UV (MeOH) λ_{max} (log ε) = 205 (4.40), 285 (3.93) nm; ECD (MeOH) λ_{max} ($\Delta\varepsilon$) = 213 (+42.37), 246 (−5.58), 305 (−6.17) nm; HR-ESI-MS *m/z* 357.1304 [M + Na]$^+$ (Calcd. for $C_{18}H_{22}O_6Na^+$, 357.1309); ^{1}H and ^{13}C NMR data, see Table 1.

Taladipyrone B (**2**): colorless prismatic crystals; $[\alpha]_D^{25}$: +16 (*c* 0.10, MeOH); UV (MeOH) λ_{max} (log ε) = 206 (4.55), 237 (4.27), 294 (4.10) nm; ECD (MeOH) λ_{max} ($\Delta\varepsilon$) = 218 (−16.15), 247 (+3.58), 298 (+5.53) nm; HR-ESI-MS *m/z* 397.1261 [M + Na]$^+$ (Calcd. for $C_{20}H_{22}O_7Na^+$, 397.1258); ^{1}H and ^{13}C NMR data, see Table 1.

Taladipyrone C (**3**): white amorphous powders; $[\alpha]_D^{25}$: +234 (*c* 0.10, MeOH); UV (MeOH) λ_{max} (log ε) = 202 (4.46), 238 (3.98), 284 (3.86) nm; ECD (MeOH) λ_{max} ($\Delta\varepsilon$) = 247 (+21.46) nm; HR-ESI-MS *m/z* 397.1256 [M + Na]$^+$ (Calcd. for $C_{20}H_{22}O_7Na^+$, 397.1258); ^{1}H and ^{13}C NMR data, see Table 1.

Taladipyrone D (**4**): white amorphous powders; $[\alpha]_D^{25}$: −149 (*c* 0.10, MeOH); UV (MeOH) λ_{max} (log ε) = 202 (4.42), 238 (3.92), 285 (3.82) nm; ECD (MeOH) λ_{max} ($\Delta\varepsilon$) = 217 (−8.21), 244 (−14.45) nm; HR-ESI-MS *m/z* 397.1264 [M + Na]$^+$ (Calcd. for $C_{20}H_{22}O_7Na^+$, 397.1258); ^{1}H and ^{13}C NMR data, see Table 2.

Taladipyrone E (**5**): colorless needle crystals; UV (MeOH) λ_{max} (log ε) = 203 (4.44), 238 (4.07), 288 (3.88) nm; HR-ESI-MS *m/z* 413.1583 [M + Na]$^+$ (Calcd. for $C_{21}H_{26}O_7Na^+$, 413.1571); ^{1}H and ^{13}C NMR data, see Table 2; **5b**: $[\alpha]_D^{25}$: +123 (*c* 0.10, MeOH) ; ECD (MeOH) λ_{max} ($\Delta\varepsilon$) = 215 (−21.36), 285 (+13.01) nm; **5a**: $[\alpha]_D^{25}$: −159 (*c* 0.10, MeOH) ; ECD (MeOH) λ_{max} ($\Delta\varepsilon$) = 216 (+14.71), 285 (−12.49) nm.

Taladipyrone F (**6**): colorless needle crystals; UV (MeOH) λ_{max} (log ε) = 205 (4.37), 234 (4.10), 285 (3.92) nm; HR-ESI-MS *m/z* 383.1462 [M + Na]$^+$ (Calcd. for $C_{20}H_{24}O_6Na^+$, 383.1465); ^{1}H and ^{13}C NMR data, see Table 2; **6b**: $[\alpha]_D^{25}$: +14 (*c* 0.10, MeOH); ECD (MeOH) λ_{max} ($\Delta\varepsilon$) = 241 (−15.58), 272 (+3.26) nm; **6a**: $[\alpha]_D^{25}$: −20 (*c* 0.10, MeOH); ECD (MeOH) λ_{max} ($\Delta\varepsilon$) = 242 (+19.54), 271 (−2.05) nm.

Taladipyrone G (**7**): colorless needle crystals; UV (MeOH) λ_{max} (log ε) = 205 (4.45), 231 (4.16), 285 (3.96) nm; HR-ESI-MS *m/z* 383.1465 [M + Na]$^+$ (Calcd. for $C_{20}H_{24}O_6Na^+$, 383.1465); ^{1}H and ^{13}C NMR data, see Table 3; **7a**: $[\alpha]_D^{25}$: +13 (*c* 0.10, MeOH); ECD (MeOH) λ_{max} ($\Delta\varepsilon$) = 241 (−31.64), 286 (+19.00) nm; **7b**: $[\alpha]_D^{25}$: −14 (*c* 0.10, MeOH); ECD (MeOH) λ_{max} ($\Delta\varepsilon$) = 242 (+45.56), 288 (−21.16) nm.

Taladipyrone H (**8**): colorless oils; UV (MeOH) λ_{max} (log ε) = 202 (4.35), 281 (3.94) nm; HR-ESI-MS *m/z* 383.1108 [M + Na]$^+$ (Calcd. for $C_{19}H_{20}O_7Na^+$, 383.1101); ^{1}H and ^{13}C NMR data, see Table 3; **8a**: $[\alpha]_D^{25}$: +82 (*c* 0.10, MeOH); ECD (MeOH) λ_{max} ($\Delta\varepsilon$) = 207 (+20.88), 243 (+0.77), 269 (+10.55), 296 (−12.11) nm; **8b**: $[\alpha]_D^{25}$: −76 (*c* 0.10, MeOH); ECD (MeOH) λ_{max} ($\Delta\varepsilon$) = 207 (−27.00), 245 (−7.38), 270 (−16.94), 300 (+3.75) nm.

Taladipyrone I (**9**): white amorphous powders; $[\alpha]_D^{25}$: +14 (*c* 0.10, MeOH); UV (MeOH) λ_{max} (log ε) = 205 (4.14), 224 (3.80), 285 (3.52) nm; ECD (MeOH) λ_{max} ($\Delta\varepsilon$) = 204 (−17.72), 233 (+3.13), 291 (+6.37) nm; HR-ESI-MS *m/z* 357.1305 [M + Na]$^+$

(Calcd. for $C_{18}H_{22}O_6Na^+$, 357.1309); ^1H and ^{13}C NMR data, see Table 3.

4.5. X-ray crystal structure analysis

Crystals of compounds **1**, **2**, **5**, **6**, and **7** were both obtained from CH_2Cl_2–MeOH–H_2O (20∶10∶1) at 4 °C. Crystallographic Data Center (CCDC) with deposition numbers CCDC 2482043 for **1**, CCDC 2482041 for **2**, CCDC 2482044 for **5**, CCDC 2482045 for **6**, and CCDC 2482042 for **7**. Copies of the data can be obtained free of charge from the CCDC, 12 Union Road, Cambridge CB 1EZ, UK [fax: Int. +44(0)-(1223)-336 033); e-mail: deposit@ccdc.cam.ac.uk].

Crystal data for compound **1**: $C_{18}H_{22}O_6$, M = 334.35, a = 12.738 10 (10) Å, b = 15.211 30 (10) Å, c = 17.386 50 (10) Å, α = 90°, β = 90°, γ = 90°, V = 3368.86 (4) Å^3, T = 293 (2) K, space group $P2_12_12_1$, Z = 8, μ(Cu Kα) = 0.821 mm^{-1}, 42 288 reflections measured, 6788 independent reflections (R_{int} = 0.0294). The final R_1 values were 0.0265 [$I > 2\sigma(I)$]. The final $wR(F^2)$ values were 0.0685 [$I > 2\sigma(I)$]. The final R_1 values were 0.0267 (all data). The final $wR(F^2)$ values were 0.0687 (all data). The goodness of fit on F^2 was 1.079. Flack parameter = −0.03 (2) (CCDC 2482043).

Crystal data for compound **2**: $C_{20}H_{22}O_7$, M =374.37, a = 7.988 41 (5) Å, b = 8.649 79 (6) Å, c = 26.536 24 (15) Å, V = 1833.602 (19) Å^3, α = 90°, β = 90°, γ = 90°, T = 100.00 (10) K, space group $P2_12_12_1$, Z = 4, μ(Cu Kα) = 0.860 mm^{-1}, 25 237 reflections measured, 3685 independent reflections (R_{int} = 0.0230). The final R_1 values were 0.0234 [$I > 2\sigma(I)$]. The final $wR(F^2)$ values were 0.0617 [$I > 2\sigma(I)$]. The final R_1 values were 0.0235 (all data). The final $wR(F^2)$ values were 0.0617 (all data). The goodness of fit on F^2 was 1.054. Flack parameter was 0.00 (3) (CCDC 2482041).

Crystal data for compound **5**: $C_{21}H_{26}O_7$, M = 390.42, a = 7.530 (2) Å, b = 7.995 (2) Å, c = 18.020 (5) Å, α = 91.500 (11)°, β = 93.925 (11)°, γ = 116.649 (11)°, V = 965.3 (5) Å^3, T = 200 (2) K, space group P-1, Z = 2, μ = 0.532 mm^{-1}, 65 999 reflections measured, 5771 independent reflections (R_{int} = 0.0686). The final R_1 values were 0.0494 [$I > 2\sigma(I)$]. The final $wR(F^2)$ values were 0.1344 [$I > 2\sigma(I)$]. The final R_1 values were 0.0552 (all data). The final $wR(F^2)$ values were 0.1371 (all data). The goodness of fit on F^2 was 1.130 (CCDC 2482044).

Crystal data for compound **6**: $C_{20}H_{24}O_6$, M = 360.39, a = 8.4067 (7) Å, b = 14.3986 (13) Å, c = 30.036 (3) Å, α = 90°, β = 93.795 (2)°, γ = 90°, V = 3627.7 (5) Å^3, T = 100 (1) K, space group $P2_1/c$, Z = 8, μ = 0.511 mm^{-1}, 93 014 reflections measured, 8436 independent reflections (R_{int} = 0.0496). The final R_1 values were 0.0421 [$I > 2\sigma(I)$]. The final $wR(F^2)$ values were 0.1099 [$I > 2\sigma(I)$]. The final R_1 values were 0.0461 (all data). The final $wR(F^2)$ values were 0.1113 (all data). The goodness of fit on F^2 was 1.082 (CCDC 2482045).

Crystal data for compound **7**: $C_{20}H_{24}O_6$, M = 360.39, a = 8.2726 (10) Å, b = 9.6175 (11) Å, c = 12.7615 (15) Å, α = 109.627 (3)°, β = 92.267 (4)°, γ = 99.416 (4)°, V = 938.56 (19) Å^3, T = 100.00 K, space group P-1, Z = 2, μ = 0.494 mm^{-1}, 25 199 reflections measured, 4394 independent reflections (R_{int} = 0.0354). The final R_1 values were 0.0362 [$I > 2\sigma(I)$]. The final $wR(F^2)$ values were 0.0964 [$I > 2\sigma(I)$]. The final R_1 values were 0.0394 (all data). The final $wR(F^2)$ values were 0.0983 (all data). The goodness of fit on F^2 was 1.033 (CCDC 2482042).

4.6. Cell culture and reagents

Human derived AC16 cells were obtained from the Servicebio (Wuhan, China). Commercially available kits to evaluate adenosine-triphosphate (ATP), lactate dehydrogenase (LDH), and malondialdehyde (MDA) content and content protein assay kit were supplied by Beyotime (Shanghai, China). Antibodies against PI3K (A4992), AKT (A18675), p-AKT (AP0637), β-actin (AC026), and HRP-conjugated goat anti-rabbit IgG (AS014) were purchased from ABclonal (Wuhan, China), while the antibody against p-PI3K (#4228S) was obtained from Cell Signaling Technology (Danvers, MA, USA).

4.7. Cell counting kit-8 (CCK-8) assay

A commercial CCK-8 kit (Beyotime, Shanghai, China) was used to detect cell viability of AC16 cells stored in 0 °C UW solution with or without compounds (40 μmol·L^{-1}) according to the manufacturer's protocol. The absorbance at 450 nm was recorded.

4.8. Apoptosis analysis

The apoptotic induction effect of compound **2** was identified *via* FITC-Annexin V/PI apoptosis detection Kit (Zoman, Beijing, China). Briefly, AC16 cells were stored in 0 °C UW solution containing DMSO (< 0.1%) or compound **2** (10, 20 or 40 μmol·L^{-1}) for 24 h. Afterward, cells were harvested and washed with PBS and resuspended in binding buffer with Annexin V-FITC and PI. Cells were subjected to flow cytometry analysis (Becton Dickinson, CA, USA) after 15 min.

4.9. Determination of ATP, LDH, and MDA

The levels of adenosine triphosphate (ATP), lactate dehydrogenase (LDH), and malondialdehyde (MDA) in AC16 cells were measured using detection kits (Bioyotime, Shanghai, China) in accordance with the manufacturer's instructions. Briefly, the AC16 cells were lysed, and the supernatant was collected after centrifugation. ATP levels were measured using a luminescence-based assay kit. LDH activity was determined by a colorimetric method at 340 nm. MDA levels were assessed using a colorimetric assay at 532 nm.

4.10. Detection of reactive oxygen species (ROS)

A commercial fluorescent probe DCFH-DA (Sigma-Aldrich, St. Louis, MO, USA) was used to determine intracellular ROS content. Briefly, AC16 cells stored in 0 °C UW solution with or without compound **2** were washed and incubated with DCFH-DA for 25 min and then washed for imaging using a Carl Zeiss Microscopy system.

4.11. Western blot analysis

Following treatment with either vehicle control (DMSO, < 0.1%) or compound **2**, cells were lysed using RIPA lysis buffer (Beyotime, Shanghai, China). Protein concentration was determined with a bicinchoninic acid (BCA) assay kit. Equal amounts of protein samples were separated by 4%–12% SDS-polyacrylamide gel electrophoresis and transferred onto PVDF membranes. The membranes were incubated with primary antibodies against PI3K, p-PI3K, AKT, p-AKT, and β-actin, followed by appropriate secondary antibodies. Protein band signals were visualized and quantified using ImageJ software (National Institutes of Health), as previously described [46].

4.12. Statistical analysis

Graph Pad Prism version 10.0 (GraphPad Software Inc., San Diego, CA, USA) was used for data analysis. All data were represented as mean ± standard deviation (SD) from three independent experiments. Multiple-group comparisons were evaluated by one-way ANOVA with post hoc testing. $P < 0.05$ was considered statistically significant ($^*P < 0.05$, $^{**}P < 0.01$, $^{***}P < 0.001$).

Funding

This work was supported by the National Natural Science Foundation of China (Nos. 82273811, 22577033, and U22A20380), the National Program for Support of Top-notch Young Professionals (No. 0106514050), the Hubei Provincial Natural Science Foundation of China (No. 2024AFA028), the Basic Research Support Program of HUST (No. 2025BRA015), the Open Fund of Hubei Jiangxia Laboratory, and the National Key Research and Development Program of China (No. 2021YFA0910500).

Supporting information

Chiral HPLC separation of racemic compounds **5–8**; 1D and 2D NMR, HR-ESI-MS, UV data of **1–9**, and experimental ECD curves of compounds **1–3**; ECD and NMR calculation details, including conformational analysis and atomic coordinates of the calculated compounds were provided. Supplementary material related to this article can be requested by sending E-mail to the corresponding authors.

Declaration of competing interest

These authors have no conflict of interest to declare.

Acknowledgments

We thank the Analytical and Testing Center at Huazhong University of Science and Technology (HUST) for measuring ECD, IR, and single-crystal X-ray diffraction data. Thanks also for the technical support by the Medical Subcenter of HUST Analytical & Testing Center.

References

1 Luo Z, Yin F, Wang X, et al. Progress in approved drugs from natural product resources. *Chin J Nat Med*. 2024;22(3):195-211. https://doi.org/10.1016/S1875-5364(24)60582-0.
2 Hu YJ, Li LX, Han JC, et al. Recent advances in the total synthesis of natural products containing eight-membered carbocycles (2009–2019). *Chem Rev*. 2020;120:5910-5953. https://doi.org/10.1021/acs.chemrev.0c00045.
3 Zhang H, Tang X. Combining microbial and chemical syntheses for the production of complex natural products. *Chin J Nat Med*. 2022;20(10):729-736. https://doi.org/10.1016/S1875-5364(22)60191-2.
4 Benjamin CR. Ascocarps of *Aspergillus* and *Penicillium*. *Mycologia*. 1955;47:669-687. https://doi.org/10.1080/00275514.1955.12024485.
5 Shi Y, Sun XQ, Zhang JX, et al. New cytotoxic *γ*-lactam alkaloids from the mangrove-derived fungus *Talaromyces hainanensis* sp. nov. guided by molecular networking strategy. *J Agric Food Chem*. 2024;72:17431-17443. https://doi.org/10.1021/acs.jafc.4c03959.
6 Wu J, Wang W, Yang Y, et al. Phenylhydrazone alkaloids from the deep-sea cold seep-derived fungus *Talaromyces amestolkiae* HDN21-0307. *J Nat Prod*. 2024;87:1407-1415. https://doi.org/10.1021/acs.jnatprod.4c00132.
7 Zhou P, Zhang X, Dai C, et al. Talaromynoids A–E: five new fusicoccane diterpenoids from the endophytic fungus *Talaromyces* sp. DC-26. *J Org Chem*. 2022;87:7333-7341. https://doi.org/10.1021/acs.joc.2c00528.
8 Dewa AA, Khalil ZG, Hussein WM, et al. Pullenvalenes A–D: nitric oxide-mediated transcriptional activation (NOMETA) enables discovery of triterpene aminoglycosides from Australian termite nest-derived fungi. *J Nat Prod*. 2024;87:935-947. https://doi.org/10.1021/acs.jnatprod.3c01233.
9 Zong S, Zhang Y, Xiao J, et al. Talauromides A–G, nitrogen-containing heptacyclic oligophenalenone dimers from the soil fungus *Talaromyces stipitatus* BMC-16. *J Nat Prod*. 2024;87:2450-2458. https://doi.org/10.1021/acs.jnatprod.4c00742.
10 Chen C, Wang X, Fang W, et al. Talaketides A–G, linear polyketides with prostate cancer cytotoxic activity from the mangrove sediment-derived fungus *Talaromyces* sp. SCSIO 41027. *Chin J Nat Med*. 2024;22(11):1047-1056. https://doi.org/10.1016/S1875-5364(24)60659-X.
11 Aguilar-Ramírez E, Reyes-Pérez V, Fajardo-Hernández CA, et al. Harnessing the reactivity of duclauxin toward obtaining hPTP1B1–400 inhibitors. *J Med Chem*. 2023;66:16222-16234. https://doi.org/10.1021/acs.jmedchem.3c01594.
12 Jiménez-Arreola BS, Aguilar-Ramírez E, Cano-Sánchez P, et al. Dimeric phenalenones from *Talaromyces* sp. (IQ-313) inhibit hPTP1B1–400: insights into mechanistic kinetics from *in vitro* and *in silico* studies. *Bioorg Chem*. 2020;101:103893. https://doi.org/10.1016/j.bioorg.2020.103893.
13 Wang G, Li Z, Wu J, et al. Mining of meroterpenoids with anti-inflammatory activity from the mangrove endophytic fungus *Talaromyces* sp. JNQQJ-4 by genome analysis and molecular network strategy. *Org Lett*. 2025;27:1662-1667. https://doi.org/10.1021/acs.orglett.5c00038.
14 Zhao JY, Wang XJ, Liu Z, et al. Nonadride and spirocyclic anhydride derivatives from the plant endophytic fungus *Talaromyces purpurogenus*. *J Nat Prod*. 2019;82:2953-2962. https://doi.org/10.1021/acs.jnatprod.9b00210.
15 Liang X, Huang ZH, Shen WB, et al. Talaromyoxaones A and B: unusual oxaphenalenone spirolactones as phosphatase inhibitors from the marine-derived fungus *Talaromyces purpureogenus* SCSIO 41517. *J Org Chem*. 2021;86:12831-12839. https://doi.org/10.1021/acs.joc.1c01452.
16 Cho Y, Park KH, Kim E, et al. Talaromides A–C, bioactive cyclic heptapeptides from *Talaromyces siglerae* isolated from a marine sponge. *J Nat Prod*. 2024;87:1230-1234. https://doi.org/10.1021/acs.jnatprod.3c01227.
17 Zhang Z, He X, Zhang G, et al. Inducing secondary metabolite production by combined culture of *Talaromyces aculeatus* and *Penicillium variabile*. *J Nat Prod*. 2017;80:3167-3171. https://doi.org/10.1021/acs.jnatprod.7b00417.
18 Liu Y, Chen KL, Zhao JY, et al. A derivative of trihydroxynaphthalenone and a pyrone metabolite from the endophytic fungus *Talaromyces purpurpgenus*. *J Asian Nat Prod Res*. 2024;26:555-561. https://doi.org/10.1080/10286020.2024.2333359.
19 Long H, Liu M, Guan S, et al. Bioactive secondary metabolites from *Talaromyces rugulosus* GIZ45-A37 and their anti-inflammatory activity. *Nat Prod Res*. 2025;40(1):266-271. https://doi.org/10.1080/14786419.2024.2446710.
20 Jia DX, Li Y, Liu XY, et al. Talaromyketides A–I: nine polyketides with anti-inflammatory activity from a soil fungus *Talaromyces* sp. KYS-41. *Bioorg Chem*. 2025;153:108275. https://doi.org/10.1016/j.bioorg.2025.108275.
21 Zheng M, Zhou C, Liao H, et al. Enantiomeric *α*-pyrone derivatives with immunosuppressive activity from *Talaromyces adpressus*. *Phytochemistry*. 2024;218:113931. https://doi.org/10.1016/j.phytochem.2023.113931.
22 Huang X, Li D, Long B, et al. Activation of a silent gene cluster from the endophytic fungus *Talaromyces* sp. unearths cryptic azaphilone metabolites. *J Agric Food Chem*. 2024;72:15801-15810. https://doi.org/10.1021/acs.jafc.4c03162.
23 Aron AT, Gentry EC, McPhail KL, et al. Reproducible molecular networking of untargeted mass spectrometry data using GNPS. *Nat Protoc*. 2020;15:1954-1991. https://doi.org/10.1038/s41596-020-0317-5.
24 Li C, Nitka MV, Gloer JB, et al. Annularins A–H: new polyketide metabolites from the freshwater aquatic fungus *Annulatascus triseptatus*. *J Nat Prod*. 2003;66:1302-1306. https://doi.org/10.1021/np030225y.
25 Zhou WY, Xi ZH, Du NN, et al. Rapid discovery of two unprecedented meroterpenoids from *Daphne altaica* Pall. using molecular networking integrated with MolNetEnhancer and network annotation propagation. *Chin Chem Lett*. 2024;35:109030. https://doi.org/10.1016/j.cclet.2023.109030.
26 Watrous J, Roach P, Alexandrov T, et al. Mass spectral molecular networking of living microbial colonies. *Proc Natl Acad Sci U S A*. 2012;109:E1743-E1752. https://doi.org/10.1073/pnas.1203689109.
27 Nothias LF, Petras D, Schmid R, et al. Feature-based molecular networking in the GNPS analysis environment. *Nat Methods*. 2020;17:905-908. https://doi.org/10.1038/s41592-020-0933-6.
28 Dong C, Wang H, Xu K, et al. LC-MS/MS-guided discovery of herbicidal himeic acid derivatives from the *Nicotiana tabacum*-derived fungus *Aspergillus japonicus* 334. *J Agric Food Chem*. 2025;73:21463-21472. https://doi.org/10.1021/acs.jafc.5c07469.
29 He QF, Wu ZL, Li L, et al. Discovery of neuritogenic securinega alkaloids from *Flueggea suffruticosa* by a building blocks-based molecular network strategy. *Angew Chem Int Ed*. 2021;60:19591-19595. https://doi.org/10.1002/anie.202103878.
30 Lin S, Zhang X, Wang H, et al. Diasperonins A–F: anti-inflammatory aspertetronin dimers discovered *via* BBMN and heterologous expression strategy. *Org Lett*. 2025;27:5435-5439. https://doi.org/10.1021/acs.orglett.5c01397.
31 Peng Y, Luo S, Li Q, et al. Discovery of indole alkaloids crienamides A and B from *Penicillium citrinum* by a simulated MS/MS-guided molecular network strategy. *Org Lett*. 2025;27:3673-3678. https://doi.org/10.1021/acs.orglett.5c00564.
32 Zhang M, Otsuki K, Tan L, et al. Automated annotation of complex natural products using a modular fragmentation-based structure assembly (MFSA) strategy. *Sci Adv*. 2025;11:eadw4693. https://doi.org/10.1126/sciadv.adw4693.
33 Cui YY, Jin Y, Sun RN, et al. The first discovery of marine polyoxygenated cembranolides as potential agents for the treatment of ulcerative colitis. *J Med Chem*. 2024;67:12248-12260. https://doi.org/10.1021/acs.jmedchem.4c00950.
34 Duan ZK, Wang X, Lian MY, et al. Bioassay-guided and DeepSAT-driven precise mining of monoterpenoid coumarin derivatives with antifeedant effects from the leaves of *Ailanthus altissima*. *J Agric Food Chem*. 2024;72:10958-10969. https://doi.org/10.1021/acs.jafc.4c01049.
35 Duan ZK, Lian MY, Dong SH, et al. Rapid discovery and biomimetic syntheses of two unusual hemiterpene-quassinoid adducts from *Brucea javanica*. *Chin Chem Lett*. 2025;37:111321. https://doi.org/10.1016/j.cclet.2025.111321.
36 Lai CR, Jiang MX, Tian DM, et al. Targeted isolation of *ω*-3 polyunsaturated fatty acids from the marine dinoflagellate *Prorocentrum lima* using DeepSAT and LC-MS/MS and their high activity in promoting microglial functions. *Mar Drugs*. 2025;23:286. https://doi.org/10.3390/md23070286.
37 Kim HW, Zhang C, Reher R, et al. DeepSAT: learning molecular structures from nuclear magnetic resonance data. *J Cheminf*. 2023;15:71. https://doi.org/10.1186/s13321-023-00738-4.
38 Reher R, Kim HW, Zhang C, et al. A convolutional neural network-based approach for the rapid annotation of molecularly diverse natural products. *J Am Chem Soc*. 2020;142:4114-4120. https://doi.org/10.1021/jacs.9b13786.
39 Ryu B, Glukhov E, Teixeira TR, et al. The kavaratamides: discovery of linear

lipodepsipeptides from the marine cyanobacterium *Moorena bouillonii* using a comparative chemogeographic analysis. *J Nat Prod*. 2024;87:1601-1610. https://doi.org/10.1021/acs.jnatprod.4c00242.
40 Luo JG, Wang XB, Xu YM, et al. Delitschiapyrone A, a pyrone–naphthalenone adduct bearing a new pentacyclic ring system from the leaf-associated fungus *Delitschia* sp. FL1581. *Org Lett*. 2014;16:5944-5947. https://doi.org/10.1021/ol502973c.
41 Bai Y, Ma X, Ren D, et al. Peniapyrones A–I, cytotoxic tricyclic-fused α-pyrone derivatives from an endophytic *Penicillium brefeldianum* F4a. *J Nat Prod*. 2024;87:1643-1651. https://doi.org/10.1021/acs.jnatprod.4c00383.
42 Li Q, Zheng M, Li F, et al. Talarolactones A–G, α-pyrone dimers with anti-inflammatory activities from *Talaromyces adpressus*, and their biosynthetic pathways. *Org Lett*. 2023;25:1616-1621. https://doi.org/10.1021/acs.orglett.2c04352.
43 Zheng M, Zhao X, Zhou C, et al. (±)-Talapyrones A–F: six pairs of dimeric polyketide enantiomers with unusual 6/6/6 and 6/6/6/5 ring systems from *Talaromyces adpressus*. *Chin J Nat Med*. 2025;23(8):932-937. https://doi.org/10.1016/S1875-5364(25)60928-9.
44 Jin X, Chi J, Zhao Y, et al. Indoloquinazoline alkaloids with cardiomyocyte protective activity against cold ischemic injury from *Aspergillus clavatonanicus*. *Bioorg Chem*. 2023;135:106482. https://doi.org/10.1016/j.bioorg.2023.106482.
45 Lin S, Zeng H, Wang C, et al. Discovery of novel natural cardiomyocyte protectants from a toxigenic fungus *Stachybotrys chartarum*. *Bioorg Chem*. 2024;149:107461. https://doi.org/10.1016/j.bioorg.2024.107461.
46 Lin S, Chai Z, Zeng H, et al. Atranones and dolabellanes with cardiomyocyte protective activity against cold ischemic injury from a coral-associated fungus *Stachybotrys chartarum*. *Phytochemistry*. 2024;226:114199. https://doi.org/10.1016/j.phytochem.2024.114199.
47 Lan H, Zheng Q, Wang K, et al. Cinnamaldehyde protects donor heart from cold ischemia-reperfusion injury *via* the PI3K/AKT/mTOR pathway. *Biomed Pharmacother*. 2023;165:114867. https://doi.org/10.1016/j.biopha.2023.114867.
48 Tan X, Chen YF, Zou SY, et al. ALDH2 attenuates ischemia and reperfusion injury through regulation of mitochondrial fusion and fission by PI3K/AKT/mTOR pathway in diabetic cardiomyopathy. *Free Radic Biol Med*. 2023;195:219-230. https://doi.org/10.1016/j.freeradbiomed.2022.12.097.
49 Zhao H, Zhang M, Zhou FX, et al. Cinnamaldehyde ameliorates LPS-induced cardiac dysfunction *via* TLR4-NOX4 pathway: the regulation of autophagy and ROS production. *J Mol Cell Cardiol*. 2016;101:11-24. https://doi.org/10.1016/j.yjmcc.2016.10.017.
50 Sedighi M, Nazari A, Faghihi M, et al. Protective effects of cinnamon bark extract against ischemia-reperfusion injury and arrhythmias in rat. *Phytother Res*. 2018;32:1983-1991. https://doi.org/10.1002/ptr.6127.
51 Liang S, Wang Y, Liu Y. Dexmedetomidine alleviates lung ischemia-reperfusion injury in rats by activating PI3K/Akt pathway. *Eur Rev Med Pharmacol Sci*. 2019;23:370-377. https://doi.org/10.26355/eurrev_201901_16785.
52 El-Maadawy WH, Hassan M, Hafiz E, et al. Co-treatment with esculin and erythropoietin protects against renal ischemia–reperfusion injury *via* P2X7 receptor inhibition and PI3K/Akt activation. *Sci Rep*. 2022;12:1-12. https://doi.org/10.1038/s41598-022-09970-8.
53 Lu T, Li H, Zhou Y, et al. Neuroprotective effects of alisol A 24-acetate on cerebral ischaemia-reperfusion injury are mediated by regulating the PI3K/AKT pathway. *J Neuroinflammation*. 2022;19:37. https://doi.org/10.1186/s12974-022-02392-3.
54 Zhang RJ, Zhang L, Manaenko A, et al. Helium preconditioning protects mouse liver against ischemia and reperfusion injury through the PI3K/Akt pathway. *J Hepatol*. 2014;61:1048-1055. https://doi.org/10.1016/j.jhep.2014.06.020.
55 Wu MP, Zhang YS, Zhou QM, et al. Higenamine protects ischemia/reperfusion-induced cardiac injury and myocyte apoptosis through activation of β_2-AR/PI3K/AKT signaling pathway. *Pharmacol Res*. 2016;104:115-123. https://doi.org/10.1016/j.phrs.2015.12.032.
56 Zhang J, Luan ZL, Huo XK, et al. Direct targeting of sEH with alisol B alleviated the apoptosis, inflammation, and oxidative stress in cisplatin-induced acute kidney injury. *Int J Biol Sci*. 2023;19:294-310. https://doi.org/10.7150/ijbs.78097.
57 Zhang J, Zhang M, Huo XK, et al. Macrophage inactivation by small molecule wedelolactone *via* targeting sEH for the treatment of LPS-induced acute lung injury. *ACS Cent Sci*. 2023;21:440-456. https://doi.org/10.1021/acscentsci.2c01424.
58 Sun CP, Zhou JJ, Yu ZL, et al. Kurarinone alleviated Parkinson's disease *via* stabilization of epoxyeicosatrienoic acids in animal model. *Proc Natl Acad Sci U S A*. 2022;119:e2118818119. https://doi.org/10.1073/pnas.2118818119.
59 Zhang J, Zhang HL, Xu XR, et al. Targeting PBK with small-molecule 1-*O*-acetyl-4*R*,6*S*-britannilactone for the treatment of neuroinflammation. *Proc Natl Acad Sci U S A*. 2025;122:e2502593122. https://doi.org/10.1073/pnas.2502593122.